Detailed dendritic excitatory/inhibitory balance through heterosynaptic spike-timing-dependent plasticity

(short title) **Heterosynaptic spike-timing-dependent plasticity**

Naoki Hiratani* and Tomoki Fukai
Laboratory for Neural Circuit Theory, RIKEN Brain Science Institute, Wako, Saitama, Japan
*N.Hiratani@gmail.com

Abstract

Balance between excitatory and inhibitory inputs is a key feature of cortical dynamics. Such balance is arguably preserved in dendritic branches, yet its underlying mechanism and functional roles are still unknown. Here, by considering computational models of heterosynaptic spike-timing-dependent plasticity (STDP), we show that the detailed excitatory/inhibitory balance on dendritic branch is robustly achieved through heterosynaptic interaction between excitatory and inhibitory synapses. The acquired dendritic balance enables neuron to perform change detection, due to functional specialization at each branch. Furthermore, heterosynaptic STDP explains how maturation of inhibitory neurons modulates selectivity of excitatory neurons in critical period plasticity of binocular matching. Our results propose heterosynaptic STDP as a critical factor in synaptic organization and resultant dendritic computation.

Introduction

Activity dependent synaptic plasticity is essential for learning. Especially, spike time difference between presynaptic and postsynaptic neurons is a crucial factor for synaptic learning (Bi and Poo, 1998)(Caporale and Dan, 2008). Recent experimental results further revealed that the relative spike timings among neighboring synapses on a dendritic branch have significant influence on changes in synaptic efficiency of these synapses (Tsukada et al., 2005)(Hayama et al., 2013)(Paille et al., 2013)(Oh et al., 2015)(Bazelot et al., 2015). Especially, the timing of GABAergic input exerts a great impact on synaptic plasticity at nearby glutamatergic synapses. Similar phenomenon were also observed in biophysical simulations (Cutsuridis, 2011)(Bar-Ilan et al., 2013). This heterosynaptic form of spike-timing-dependent plasticity (h-STDP) is potentially important for synaptic organization on dendritic tree, and resultant dendritic computation (Mel and Schiller, 2004)(Branco et al., 2010). However, the functional role of h-STDP remains elusive, partly due to lack of simple analytical model.

In the understanding of homosynaptic STDP, simple mathematical formulation of plasticity has been playing important roles (Gerstner et al., 1996)(Song et al., 2000)(Vogels et al., 2011). Motivated by these studies, we constructed a mathematical model of h-STDP based on calcium-based synaptic plasticity models (Shouval et al., 2002)(Graupner and Brunel, 2012), and then considered potential functional merits of the plasticity. The model reproduces the several effects of h-STDP observed in the hippocampal CA1 area and the striatum of rodents (Hayama et al., 2013)(Paille et al., 2013), and provides analytical insights for the underlying mechanism. The model further indicates that h-STDP causes the detailed balance between excitatory and inhibitory inputs on a dendritic branch owing to the correlated inhibitory inputs that shunt long-term depression (LTD) at neighboring excitatory synapses. This result suggests that not only the number and the total current of excitatory/inhibitory synapses are balanced at a branch (Liu, 2004)(Wilson et al., 2007), but temporal input structure is also balanced as observed in the soma (Dorrn et al., 2010)(Froemke, 2015). Moreover, by considering detailed single neuron models, we show that such detailed balance is beneficial for detecting changes in input activity. The model also reconciles with critical period plasticity of binocular matching observed in V1 of mice (Wang et al., 2010)(Wang et al., 2013), and provides a candidate explanation on how GABA-maturation modulates the selectivity of excitatory neurons during development.

Results

Calcium-based synaptic plasticity model with current-based heterosynaptic interaction explains h-STDP.

We constructed a model of a dendritic spine as shown in Fig. 1A (see *Model* A_1 in Methods for details). In the model, the membrane potential of the spine $u(t)$ is modulated by influx/outflux from AMPA/NMDA receptors (x^A and $g_N(u)x^N$ in Fig. 1A), back-propagation (x^{BP}), and heterosynaptic currents from nearby excitatory/inhibitory synapses (x^E and x^I). Calcium concentration in the spine $c(t)$ is controlled through NMDA receptors and voltage-dependent calcium channels (VDCC) (Higley and Sabatini, 2012). Because, both NMDA and VDCC are voltage-dependent (Lüscher and Malenka, 2012), the calcium level in the spine is indirectly controlled by pre, post, and heterosynaptic activities (Fig. 1B top and middle panels). For synaptic plasticity, we used calcium-based plasticity model, in which LTP/LTD are initiated if the Ca^{2+} level is above LTP/LTD thresholds (orange and cyan lines in Fig. 1B middle). This plasticity model is known to well capture homosynaptic STDP (Shouval et al., 2002)(Graupner and Brunel, 2012). We introduced an intermediate variable $y(t)$ to capture non-graded nature of synaptic weight change (Petersen et al., 1998). Thus, changes in Ca^{2+} level are first embodied in the intermediate $y(t)$ (Fig. 1B bottom), and then reflected to the synaptic weight $w(t)$ upon accumulation. The intermediate variable $y(t)$ is expected to correspond with concentration of plasticity related enzymes such as CaMKII or PP1 (Graupner and Brunel, 2007).

We first consider the effect of inhibitory input to synaptic plasticity at nearby excitatory spines. A recent experimental result revealed that, in medium spiny neuron, a synaptic connection from a cortical excitatory neuron typically shows anti-Hebbian type STDP under pairwise stimulation protocol, but if GABA-A receptor is blocked, STDP time window flips to Hebbian (Paille et al., 2013) (points in Fig. 2A). The proposed model can explain this phenomenon in the following way. Let us first consider the case when the presynaptic excitatory input arrives before the postsynaptic spike. If the GABAergic input is blocked, presynaptic and postsynaptic spikes jointly cause a large membrane depolarization at the excitatory spine. Subsequently, the calcium concentration rises up above the LTP threshold (red line in Fig 2B upper-right), hence inducing LTP after repetitive stimulation (red line in Fig 2B lower-right). In contrast, if the GABAergic input arrives coincidentally with the presynaptic input, depolarization at the excitatory spine is attenuated by negative current influx though the inhibitory synapse. As a result, calcium concentration cannot go up beyond the LTP threshold although it is still high enough to eventually cause LTD (black lines in Fig 2B right). Similarly when the postsynaptic spike arrives to the spine before the presynaptic spike does, without any GABAergic input, the presynaptic spike causes slow decay in the level of calcium concentration that may induce LTD (red lines in Fig 2B left). On the contrary, if the GABAergic input is provided simultaneously with the presynaptic input, slow decay in the calcium concentration is blocked because the inhibitory input causes hyperpolarization of the membrane potential at the excitatory spine. As a result, LTP is more likely achieved (black lines in Fig. 2B left). Therefore, when a GABAergic input arrives in coincidence with a presynaptic excitatory input, the STDP time window changes its sign in both pre-post and post-pre regimes (lines in Fig. 2A).

GABAergic effect on excitatory synaptic plasticity is also observed in CA1 (Hayama et al., 2013). In this case, post-pre stimulation does not induce LTD unless GABA uncaging is conducted near the excitatory spine right before the postsynaptic spike arrives at the spine, whereas LTP is induced by pre-post stimulation regardless of GABA uncaging (blue and cyan points in Fig. 2C). The proposed model can also replicate these results. In pre-post stimulation, due to positive feedback through NMDA receptor, the membrane potential of the spine shows strong depolarization even if inhibitory current is delivered through GABA uncaging (blue lines in Fig. 2D upper-right). Thus, LTP is caused after repetitive stimulation (blue lines in Fig. 2D lower-right). By contrast, in post-pre protocol, LTP/LTD effects tend to cancel each other in the absence of GABAergic input, whereas LTD becomes dominant under the influence of GABAergic input (blue lines in Fig. 2D left).

In addition to inhibitory-to-excitatory effect, excitatory-to-excitatory (E-to-E) effect is also observed in case of CA1 (Hayama et al., 2013). If GABA uncaging is performed right before postsynaptic firing, LTD is also observed in neighboring excitatory spines (green point in Fig. 2C right). This E-to-E heterosynaptic effect is not observed in the absence of GABAergic input (compare green points in Fig 2C left). Correspondingly, in the model, excitatory current influx from a nearby synapse causes mild potentiation of calcium concentration in cooperation with inhibitory current influx, hence eventually induces LTD (green lines in Fig 2D left). Note that for this E-to-E effect, interaction at latter stage of synaptic plasticity may also play a dominant role (Hayama et al., 2013).

Phase transitions underlying h-STDP

In the previous section, we introduced a complicated model to establish its relevance to the corresponding biological processes and get insight into the underlying mechanism. However, not all components of the model are necessary to reproduce the observed properties of h-STDP. Here, we provide a simple analytically tractable model to investigate the generality of the proposed mechanism.

To this end, we simplify the model to the one in which calcium level at a spine is directly modulated by pre-, post-, and heterosynaptic activities as given below,

$$\frac{dC_i(t)}{dt} = -\frac{C_i(t)}{\tau_C} + C_{pre}X_i(t) + C_{post}\left[1+g_C\left(C_i(t-\Delta t)\right)\right]X_{post}(t) \\ -C_I\sum_{j\in\Omega_i^I} X_j^I(t-d_I) + C_E\sum_{j\in\Omega_i^E} X_j^E(t-d_E). \qquad (1)$$

Here, $C_i(t)$ represents Ca^{2+} concentration at spine i, X_i and X_{post} represent presynaptic and postsynaptic spikes respectively, d_I and d_E are heterosynaptic delays, and Ω_i^I and Ω_i^E are the sets of neighboring inhibitory and excitatory synapses, respectively (see *Model B* in Methods for the details of the model). Despite simplicity, the model can qualitatively reproduce heterosynaptic effects observed in striatal and CA1 neurons, though the quantitative coincidence is degraded (Fig. 3A and B respectively). Importantly, the reduced model provides further analytical insights into the phenomena.

Let us first consider how the inhibitory effect parameter C_I controls I-to-E heterosynaptic effect observed in the CA1 experiment. If we characterize the shape of STDP time windows by the total number of its local minimum/maximum, the parameter space can be divided into several different phases (Fig. 3C). If LTP threshold θ_p satisfies $C_{pre} < \theta_p < C_{post}$, Hebbian type STDP time window appears when the strength of heterosynaptic inhibitory effect C_I satisfies $\left(C_{post}-\theta_p\right)e^{\delta_I/\tau_C} < C_I < C_{pre}e^{\delta_I/\tau_C}$ (upper orange-colored region in Fig. 3C; see Methods for the details of analysis). Here we defined δ_I as the spike timing difference between inhibitory spike and presynaptic (postsynaptic) spikes in pre-post (post-pre) stimulation protocols. If C_I is larger than $C_{pre}\exp(\delta_I/\tau_C)$, a strong inhibitory effect causes LTD even in the pre-post regime (green-colored region in Fig. 3C), whereas LTD in the post-pre regime is suppressed when C_I is smaller than $(C_{pre}-\theta_p)\exp(\delta_I/\tau_C)$ (gray-colored region in Fig. 3C). Thus, heterosynaptic LTD observed in Fig.2C can be understood as the phase shift from the gray-colored region to the orange-colored region in Fig 3C, due to change in the inhibitory effect C_I. This analysis further confirms that, for induction of heterosynaptic LTD, the heterosynaptic spike timing difference δ_I should be smaller than the timescale of Ca^{2+} dynamics τ_C (Hayama et al., 2013). This is because $\delta_I < \tau_C \log\left(\frac{C_I}{C_{post}-\theta_p}\right)$ is necessary for a significant heterosynaptic LTD, and typically C_I is smaller than C_{post} and θ_p. In addition, heterosynaptic suppression of pre-post LTP (green-colored region) is very unlikely to happen because $C_I > C_{pre}\exp(\delta_I/\tau_C)$ is necessary. This condition is difficult to satisfy even if δ_I=0, because the heterosynaptic effect on Ca^{2+} dynamics in the spine is expected to be smaller than the homosynaptic effect (i.e. $C_I < C_{pre}$).

The model also provides an analytical insight to E-to-E interaction. In E-to-E interaction, neighboring synapses receive small heterosynaptic calcium transient C_E instead of presynaptic input C_{pre}. Thus, we can characterize the shapes of STDP time windows by the heterosynaptic excitatory effect parameter C_E, and postsynaptic effect parameters C_{post} (Fig. 3D). When the postsynaptic effect parameter C_{post} satisfies $\theta_p < C_{post} < \theta_p + C_I e^{-\delta_I/\tau_C}$, and the heterosynaptic effect parameter C_E fulfills $C_I e^{-\delta_I/\tau_C} < C_E < \theta_p$, STDP time window shows Hebbian-type timing dependency (upper-middle orange-colored region in Fig. 3D). On the other hand, if C_E is smaller than $C_I e^{-\delta_I/\tau_C}$ while satisfying $\theta_p + C_I e^{-\delta_I/\tau_C} - C_{post} < C_E$, then the STDP curve becomes LTD dominant (upper-left green-colored region in Fig. 3D). Excitatory heterosynaptic effect C_E is expectedly smaller than the inhibitory effect C_I, because the inhibitory potential is typically more localized (Gidon and Segev, 2012). Thus, $C_E < C_I e^{-\delta_I/\tau_C}$ is likely the case, suggesting robust heterosynaptic LTD at neighboring synapses as observed in experiments (Hayama et al., 2013)(Oh et al., 2015). These analytical results revealed that the heterosynaptic effects are always observable if the parameters of calcium dynamics fall into a certain region in the parameter space, suggesting the robustness of h-STDP in our framework.

h-STDP induces detailed dendritic E/I balance at dendritic hotspots

Results so far suggest that the proposed model gives a good approximation of h-STDP. We next study how this h-STDP rule shapes synaptic organization on the dendrite of a simulated neuron to investigate its possible functions. To this end, we first consider a model of a dendritic hotspot (Jia et al., 2010) that receives 10 excitatory inputs and one inhibitory input (Fig. 4A). Excitatory inputs are organized into 5 pairs, and each pair of excitatory synapses receives correlated inputs (Fig. 4B; see

Model A_2 in Methods for details). In addition, the inhibitory input is correlated with one excitatory pair (in Fig. 4A, blue ones). Here, we assumed that postsynaptic activity follows a Poisson process, because the influence of a single hotspot to the soma is usually negligible. In addition, we neglected the effect of morphology and hypothesized that heterosynaptic interaction occurs instantaneously within the hotspot. In this configuration, surprisingly, excitatory synapses correlated with the inhibitory input are potentiated while other synapses experience minor depression (Fig. 4C). This potentiation is only observable when inhibitory activity is tightly correlated with excitatory activities, and becomes larger when inhibitory spike precedes excitatory spikes compared to the opposite case (Fig. 4D). In addition, heterosynaptic inhibitory effect γ_I needs to be relatively small in order to have correlated potentiation (red area in Fig. 4E). Otherwise, inhibitory input causes strong hyperpolarization at nearby synapses, resulting in depression at correlated excitatory synapses rather than potentiation (blue area in Fig. 4E). These results indicate that h-STDP induces dendrite-specific detailed E/I balance by potentiating excitatory synapses correlated with inhibitory synapses.

To reveal the underlying mechanism of this E/I balance generation, from the simulation data, we calculated the probability of calcium level being above the LTD/LTP thresholds after a presynaptic spike. The probability of LTD occurrence shows similar trajectories after a presynaptic spike, regardless of whether presynaptic activity is correlated with inhibitory input or not (dotted lines in Fig. 4F). On the other hand, the maximum probability of LTD occurrence is significantly lower for spines correlated with inhibitory inputs (solid lines in Fig. 4F), although the probability goes up after the presynaptic spike in both cases. This asymmetry between LTP and LTD can be understood in the following way; LTD is mainly caused when the presynaptic neuron fires and the postsynaptic neuron remains silent both in the experiment (Malenka and Bear, 2004) and in the model (gray line in Fig. 4G). However, if inhibitory input arrives at a nearby dendrite in coincidence, calcium boost caused by excitatory presynaptic input is attenuated by heterosynaptic inhibitory effect (black line in Fig. 4G). As a result, LTD is shunted by correlated inhibitory inputs. On the other hand, LTP is mainly caused by coincidence between pre and postsynaptic spikes, which induces a large increase in calcium level that overwhelms the attenuation by the heterosynaptic inhibitory effect. Thus, inhibitory activity at a nearby site does not prevent LTP at correlated excitatory synapses (Fig. 4H). Therefore, correlated spines experiences less depression, hence tend to be potentiated as a net sum.

To check the generality of the observed dendritic E/I balance, we extended the model to a two-layered single cell (Poirazi et al., 2003) by modeling each branch with one dendritic hotspot (Fig. 5A; see *Model A_3* in Methods for details), and investigated the dendritic organization by h-STDP. Even in this case, when the postsynaptic neuron receives input from various neurons with different selectivity, each dendritic hotspot shapes its excitatory synaptic organization based on the selectivity of its inhibitory input (Fig. 5B). These result further imply that correlation-based clustering of excitatory synapses observed in previous experiments (Kleindienst et al., 2011)(Takahashi et al., 2012) are possibly caused by common inhibitory inputs instead of direct interaction among excitatory spines.

Detailed dendritic E/I balance enables robust change detection

In the previous section, we demonstrated that h-STDP induces the detailed E/I balance on dendritic branches. We next investigate the possible function of such synaptic organization in information processing. To this end, we constructed detailed single neuron models using NEURON simulator(Hines and Carnevale, 1997). Based on a previously developed model of spiny neuron in neocortical layer 4 (Mainen and Sejnowski, 1996), we built a model by distributing 200 inhibitory and 1000 excitatory synaptic inputs on the dendritic tree (Fig. 6A). As in the previous section, presynaptic neurons are selective for one of five stimuli shown by colors. In addition, inhibitory presynaptic neurons show a 5 milliseconds delay in response to the stimuli compared to the excitatory counterpart (Froemke, 2015). The detailed E/I balance was achieved by setting the stimulus selectivity of excitatory synapses such that the excitatory selectivity coincides with the selectivity of the nearest inhibitory input (left two panels in Fig. 6A; see *Model C* in Methods for details). Note that this synaptic distribution is expected to be self-organized through h-STDP (Fig. 4,5), although here we manually set the input distribution. We additionally constructed a model with random synaptic distribution (Fig. 6A middle-right), and a model with excitatory clustering without the dendritic E/I balance (Fig. 6A right), for comparing response properties with the dendritic E/I balance model.

When five stimuli are presented in a random sequential order, the neuron with the dendritic E/I balance tends to show bursting activity immediately after a stimulus is changed to the next, and stays almost silent during the rest of time (Fig 6B top). By contrast, the other two models show rather persistent spiking activity for the same input activity (Fig. 6B middle and bottom). If we compare the ratio of spikes that detect the changes (i.e. the ratio of output spike count in the gray areas of Fig. 6B to the number of total spikes), the dendritic E/I balance model robustly outperforms the other two (Fig. 6C). Moreover, the advantage remains significant even if the performance is compared at a fixed output-firing rate (Fig. 6D), suggesting that change detection is not a mere result of sparse postsynaptic activity, but a result of the dendritic E/I balance. Indeed, in the model, the membrane potential at a distal dendritic branch, which is indicated by arrows in Figure 6A, stays hyperpolarized except for the changing points (cyan line in Fig.6E top). On the contrary, in the other two models, both values show large changes depending on stimulus type, due to lack of the detailed E/I balance (green and magenta lines in Fig. 6E top). A similar tendency is also observed for the intracellular calcium concentration (Fig. 6E bottom).

In previous models on the somatic E/I balance, for sparse information processing, it was crucial that excitatory inputs arrives the neuron in the absence of strong inhibitory inputs (Kremkow et al., 2010)(Vogels et al., 2011). In contrast, in our model, inhibitory inputs from the previous stimuli remain active at the changing points due to the delay, so that the total input firing rates stay the same during stimulation, yet change detection is still achievable. This is because, in our model, each dendritic component is often specialized for detecting the onset of one or two input sources. For instance, in the dendritic component depicted in Figure 6E, orange and dark-red (1st and 3rd) stimuli are well detected. As a result, somatic potential can represent general change information through dendritic computation. These results indicate that the dendritic E/I balance is highly beneficial for change detection.

h-STDP explains critical period plasticity of binocular matching

Results so far indicate that h-STDP induces GABA-driven synaptic reorganization that enriches dendritic computation. To investigate its relationship with the developmental plasticity, we next consider a model of critical period plasticity in binocular matching (Wang et al., 2010)(Wang et al., 2013). In mice, one week after the eye opening, typically, binocular neurons in V1 still have different orientation selectivity for inputs from two eyes. Nevertheless, two more weeks after, selective orientations for both eyes get closer, and eventually they almost coincide with each other (Wang et al., 2010). Moreover, this binocular matching is disrupted by accelerating inhibitory maturation (Wang et al., 2013). Thus, expectedly, activity of inhibitory neurons play a crucial role in binocular matching in addition to Hebbian plasticity at excitatory synapses.

We modeled this process with a two-layered single cell model introduced in Fig. 5 (Fig. 7A right; see *Model* A_4 in Methods for details). Input spike trains were modeled as rate modulated Poisson processes driven by a circular variable θ, which corresponds to the direction of moving visual stimuli. We assumed followings: (i) inputs from ipsi- and contralateral eyes already have some weak orientation selectivity at the eye opening (Wang et al., 2010)(Espinosa and Stryker, 2012), (ii) Inhibitory cells are driven by both ipsi- and contralateral eyes (Yazaki-Sugiyama et al., 2009)(Kuhlman et al., 2011), (iii) The average selectivity of inhibitory inputs comes in between the selectivity for ipsilateral excitatory inputs and that for contralateral excitatory inputs (Fig. 7A left). The last assumption has not yet been supported from experimental evidence, but if inhibition is provided from neighboring interneurons, these inhibitory neurons are likely to be driven by similar sets of feedforward excitatory inputs to those driving the output neuron. Here, we consider direction selectivity instead of orientation selectivity for mathematical convenience, but the same argument holds for the latter.

In the simulation, we first run the process without inhibition then introduced GABAergic inputs after a while (red lines in Fig. 7B,E represent the starting points of inhibitory inputs), because maturation of inhibitory neurons typically occurs in a later stage of the development (Hensch, 2005). Upon the introduction of inhibition, in each branch, the mean preferred direction of excitatory synapses converges to that of the local inhibition owing to heterosynaptic plasticity (Fig. 7B top; see *Model* A_4 for details), though synaptic weight development was biased toward the selectivity of the postsynaptic neuron (Fig. 7D; here, the bias is toward the right side). This dendritic E/I balancing shrinks the difference between ipsilateral and contralateral selectivity on average, because both of them get closer to the inhibitory selectivity (Fig. 7B middle). As a result, binocular selectivity becomes stronger (Fig. 7B bottom), and the responses for monocular inputs approximately coincide with each other (Fig 7C right). Deprivation of contralateral inputs immediately after the introduction of inhibition blocks binocular matching (Fig. 7E), as expected from the experiment (Wang et al., 2010).

In addition, precocious GABA maturation is known to disrupt binocular matching (Wang et al., 2013). Our model suggests that the disruption is possibly related to the violation of the third assumption in the model. When the direction of the mean inhibitory selectivity is far different from both ipsilateral and contralateral selectivity (in Fig 7F, at the parameter regions outside of the area surrounded by purple and green lines), h-STDP does not work effectively (Fig. 7F top), and the difference between ipsi- and contralateral inputs is not reduced (Fig. 7F middle). As a result, binocular direction selectivity is not improved by learning (Fig. 7F bottom). These results indicate that GABA-maturation and resultant h-STDP are an important part of the underlying mechanisms of critical period plasticity in binocular matching.

Discussion

In this study, we first showed that a calcium-based plasticity model robustly captures several characteristics of plasticity-related interaction between neighboring synapses in millisecond timescale, by introducing heterosynaptic interaction terms (Fig. 2,3). Based on this proposed model, we next investigated the possible functions of h-STDP. Our study revealed that correlated E/I synaptic inputs on the same hotspot causes the detailed dendritic E/I balance (Fig. 4,5), which is beneficial for change detection (Fig. 6). Furthermore, we found that h-STDP can induce binocular matching upon GABA maturation, and support an accurate input estimation (Fig. 7).

Experimental predictions

Our study provides three experimental testable predictions: First, the results in Figure 4 indicate that LTD at an excitatory synapse is cancelled out by coincident inhibitory inputs to the nearby dendrite. Thus, LTD by low frequency stimuli (Malenka and Bear, 2004) can be attenuated by coincident GABA uncaging around the stimulated spine. Note that this result would not contradict with GABA-driven heterosynaptic LTD observed in paired stimulation, because in that experiment, the excitatory spine was presumably overexcited for inducing LTD in the absence of GABA (Hayama et al., 2013). Indeed, coincident GABAergic inputs may induce hetersosynaptic LTD if combined with presynaptic stimulation at a moderately high frequency that itself does not cause LTD (Blaise and Bronzino, 2003) .

Secondly, our results provide a hypothesis for synaptic organization on dendritic tree. It is known that excitatory synaptic inputs to a dendritic hotspot often show correlated activities (Kleindienst et al., 2011)(Takahashi et al., 2012). Our results indicate that an inhibitory input may also be correlated to excitatory inputs projecting to the nearby dendrite (Fig. 4,5), especially on a dendritic tree of an excitatory neuron that is sensitive to changes in the external environment (Fig. 6). Moreover, the model explains why feature selectivity of these spines only shows a weak similarity despite their correlations (Jia et al., 2010) (Chen et al., 2011). Suppose a synaptic cluster is carved by the heterosynaptic effect of common inhibitory inputs, but not by excitatory-to-excitatory interactions, variability within the cluster tends to be large, because inhibitory neurons typically have a wider feature selectivity than excitatory neurons (Ma et al., 2010)(Moore and Wehr, 2013). In addition, it should also be noted that, E-to-E heterosynaptic LTP is typically induced as a meta-plasticity in the timescale of minutes (Harvey and Svoboda, 2007), which itself is not sufficient to create a correlation-based synaptic cluster.

The third implication of the model is about binocular matching. Our model indicates that GABA-maturation plays a critical role in binocular matching, and proposes a candidate mechanism for disruption of binocular matching by precocious GABA maturation (Wang et al., 2013) (Fig. 7). However, the phenomenon can also be explained by Hebbian plasticity plus some kind of meta-plasticity. If binocular matching is purely induced by Hebbian plasticity not through heterosynaptic mechanism, selective orientation after the matching should depend solely on the initial selectivity for monocular inputs, assuming that selectivity of presynaptic neurons remains the same. Especially when the contralateral input is larger than the ipsilateral input, the resultant selectivity should approximately coincide with the original contralateral selectivity. On the other hand, if the proposed mechanism takes part in the development, the consequent selectivity should also be influenced by the mean selectivity of inhibitory input neurons. Thus, long-term imaging of monocular selectivity at binocular neurons in V1 would reveal whether a covariance-based rule is sufficient enough to explain the phenomena, or some other mechanisms including the proposed one also play a major role in the shift.

Carrier of heterosynaptic interaction

Heterosynaptic plasticity has been observed in various spatial and temporal scales, and arguably underlying molecular mechanisms are different for different spatiotemporal scales (Nishiyama and Yasuda, 2015). In the case of milliseconds-order interaction, single-atomic ions are strong candidates, because poly-atomic ions such as IP_3 are too big to move rapidly from spine to spine (Santamaria et al., 2006). Suppose that changes in Ca^{2+} concentration at an un-stimulated spine are crucial for heterosynaptic plasticity, Ca^{2+} influx/outflux from either intra or extracellular sources are necessary for induction of heterosynaptic plasticity. Because inhibitory synaptic inputs often change the local Ca^{2+} concentration in the dendritic branch (Müllner et al., 2015), intracellular spreading of Ca^{2+} may be a major source for Ca^{2+} changes in nearby un-stimulated spines. At the same time, because inhibitory inputs significantly modulate the membrane voltage of local dendrite(Gidon and Segev, 2012), a synaptic input should strongly drive Ca^{2+} influx/outflux from extracellular sources even at NMDA and VDCC of nearby un-stimulated spines. In addition, most of intracellular calcium-ions exist within calcium-buffer (Higley and Sabatini, 2012), and arguably they are also important for induction of synaptic plasticity. In our model, both current-based interaction (*Model A*) and calcium-based interaction (*Model B*) replicate the experimental results (Fig. 2 and 3, respectively). Nevertheless, our analytical study suggest that the heterosynaptic Ca^{2+} change typically needs to be comparable with the homosynaptic change in order to cause significant heterosynaptic plasticity through calcium-based interaction (Fig. 3C, D). Thus, our study implies possible importance of current-based interaction and spine specific influx/outflux of extracellular Ca^{2+} for heterosynaptic plasticity.

Note that heterosynaptic interaction does not need to work in milliseconds order to interfere with STDP. For instance, E-to-E heterosynaptic LTD can be initiated by spreading of LTD-related molecules, not by messengers of neural activity (Hayama et al., 2013). In addition, for a shift in STDP time window, changes in the ratio between calcium influx through NMDA and the influx through VDCC possibly play a crucial role (Paille et al., 2013).

Inhibitory cell types

Somatostatin positive (SOM^+) inhibitory neurons are typically projected to the apical dendrite, their IPSP curves is shorter than the timescales of NMDA or Ca^{2+} dynamics (Markram et al., 2004), and they often show strong feature selectivity compared to other inhibitory neuron types (Ma et al., 2010). Thus, this inhibitory cell type is the likely candidate for heterosynaptic STDP. However, our results do not exclude parvalbumin positive (PV^+) inhibitory neurons, which usually have projections to proximal dendrites, and also are typically fast spiking (Markram et al., 2004). In particular, h-STDP through PV^+ cell may play important roles in critical period plasticity (Takesian and Hensch, 2013).

Related theoretical studies

Previous biophysical simulation studies revealed that synaptic plasticity at excitatory synapse critically depends on inhibitory inputs at nearby dendrite (Cutsuridis, 2011)(Bar-Ilan et al., 2013)(Jedlicka et al., 2015), but these studies did not reveal the functional roles of the heterosynaptic plasticity. On the other hands, network modeling studies found that heterosynaptic plasticity provides a homeostatic mechanism (Chen et al., 2013)(Zenke et al., 2015), but in these models, heterosynaptic plasticity was modeled as a global homeostatic plasticity without any branch specificity, and the advantage over other homeostatic mechanisms was unclear. In this study, by considering intermediate abstraction with analytical but biologically plausible models, we proposed candidate mechanisms for experimental results that have not been modeled before, and revealed potential functions of h-STDP in neural circuit formation.

Methods

Model A_1: Calcium-based STDP model with current-based heterosynaptic interaction

Let us first consider membrane dynamics of a dendritic spine. Membrane potential of a spine is mainly driven by presynaptic inputs through AMPA/NMDA receptors, backpropagation of postsynaptic spike, leaky currents, and current influx/outflux caused by excitatory/inhibitory synaptic inputs at nearby synapses. Hence, we modeled membrane dynamics of spine *i* with the following differential equation:

$$\frac{du_i(t)}{dt} = -\frac{u_i(t)}{\tau_m} + \gamma_A x_i^A(t) + \gamma_N g_N(u_i) x_i^N(t) + \gamma_{BP} x_i^{BP}(t) - \gamma_I \sum_{j\in\Omega_i^I} x_j^I(t-d_I) + \gamma_E \sum_{j\in\Omega_i^E} x_j^E(t-d_E), \quad (2)$$

where u_i is the membrane potential of the spine, and τ_m is the membrane time constant. Here, conductance changes were approximated by current changes (see **Table 1** for definitions of variables). The resting potential was renormalized to zero for simplicity. In next terms, x_i^A and x_i^N are glutamate concentration on AMPA/NMDA receptors respectively. The function $g_N(u_i)=\alpha_N u_i+\beta_N$ represents voltage dependence of current influx through NMDA receptors. This positive feedback is enhanced when additional current is provided through back-propagation. As a result, the model reproduces large depolarization caused by coincident spike between presynaptic and postsynaptic neurons. Although AMPA receptor also shows voltage dependence, here we neglected the dependence, as the relative change is small around the resting potential (Lüscher and Malenka, 2012). x_i^{BP} is the effect of backpropagation from soma, and the last two term of the equation represents heterosynaptic current, which is given as the sum of inhibitory (excitatory) currents x_j^I (x_j^E) at nearby synapses. We defined sets of nearby inhibitory/excitatory synapses as Ω_i^I and Ω_i^E respectively, and their delays were denoted as d_I and d_E. Each input x_i^Q (Q = A,N,BP,I,E) is given as convoluted spikes:

$$\frac{dx_i^Q(t)}{dt} = -\frac{x_i^Q(t)}{\tau_Q} + \sum_{s^k} \delta\left(t - s^k\right), \tag{3}$$

where s^k represents the spike timing of the k-th spike. In the simulation, although convolution is calculated at the heterosynaptic synapse, this does not influence results because exponential decay is linear.

We next consider calcium influx to a spine through NMDA receptors and VDCC. For a given membrane potential u_i, calcium concentration at spine i can be written as

$$\frac{dc_i}{dt} = -\frac{c_i}{\tau_C} + g_N(u_i)x_i^N(t) + g_V(u_i), \tag{4}$$

where $g_V(u_i) = \alpha_V u_i$ represents calcium influx through VDCC, and $g_N(u_i)x_i^N(t)$ is the influx from NMDA.

Calcium concentration at spine is the major indicator of synaptic plasticity, and many results indicate that high Ca^{2+} concentration on a spine typically induces LTP, while low concentration often causes LTD (Lüscher and Malenka, 2012). Previous modeling studies revealed calcium-based synaptic plasticity model constructed on that principle well replicate various homosynaptic STDP time window observed in in vitro experiments (Shouval et al., 2002)(Graupner and Brunel, 2012). Hence, here we employed their framework for plasticity model. We additionally introduced an intermediate variable to reflect all-or-none nature of synaptic weight change (Petersen et al., 1998). This variable approximately represents the concentration of plasticity related enzymes such as CaMKII or PP1 (Graupner and Brunel, 2007). In the proposed model the intermediate y_i and synaptic weight w_i follow

$$\frac{dy_i(t)}{dt} = -\frac{y_i(t)}{\tau_y} + C_p\left[c_i - \theta_p\right]_+ - C_d\left[c_i - \theta_d\right]_+, \tag{5}$$

$$\frac{dw_i(t)}{dt} = B_p\left[y_i - y_{th}\right]_+ - B_d\left[-\left(y_i + y_{th}\right)\right]_+. \tag{6}$$

$[X]_+$ is a sign function which returns 1 if $X \geq 0$, returns 0 otherwise. Note that, in this model setting, as observed in recent experiments (Gambino et al., 2014), back-propagation is not necessary for LTP, if presynaptic inputs are given when the membrane potential at the spine is well depolarized.

In the simulation, we set common parameters as τ_C=18.0ms, τ_M=3.0ms, τ_N=15.0ms, τ_A=3.0ms, τ_{BP}=3.0ms, τ_I=3.0ms, τ_E=6.0ms, τ_Y=50s, d_I=0.0ms, α_N=1.0, α_V=2.0, γ_A=1.0, θ_p=70, θ_d=35, C_p=2.3, C_d=1.0, B_p=0.001, B_d=0.0005. In the model of STDP at striatum, in addition, we used β_N=1.0, γ_N=0.0, γ_{BP}=8.0, γ_I=5.0, y_{th}=250, while for the model of Schaffer collateral synapses, we used d_E=1.0, β_N=0.0, γ_N=0.2, γ_{BP}=8.5, γ_I=3.0, γ_E=1.0, y_{th}=750. In the parameter search, decay time constants were chosen from biologically reasonable ranges (Koch, 1998), α_N, γ_A, C_d, B_d were fixed at unitary values, and other parameters were manually tuned. Synaptic weight variables $\{w\}$ were bounded to $0 < w < 500$, and initialized at $w = 100$. All other variables were initialized at zero in the simulation. Paired stimulation was given every 1 second for 100 seconds, and synaptic weight changes were calculated from the values 400 seconds after the end of stimulation. In the cortico-striatal synapse model, the inhibitory spike was presented at the same timing with the presynaptic spike, and for Schaffer collateral synapses, inhibitory spikes were given 10 milliseconds before pre (post) spikes in pre-post (post-pre) stimulation protocols. In calculation of intermediate variable $y(t)$ in Fig. 2B,D, we ignored the effect of exponential term, because of the difference in timescale. We subtracted 7.5 milliseconds of axonal delay from the timing of presynaptic stimulation in the calculation of spike timing difference.

Model A_2: Models of a dendritic hotspot

Dendritic hotspot model was constructed based on the Schaffer collateral synapse model described above. For simplicity, we hypothesized that heterosynaptic effect by inhibitory spike arrives at excitatory spines at the same time, and also disregarded E-to-E interaction by setting γ_E=0.0. Correlated spikes were generated using hidden variables as in previous studies (Vogels et al., 2011)(Hiratani and Fukai, 2015). We generated five dynamic hidden variables, and updated them at each time step by $s_\mu(t+\Delta t) = \left(\zeta - \tfrac{1}{2}\right)\left(1-\alpha_s\right) + s_\mu(t)\alpha_s$, where $\alpha_s = \exp\left[-\Delta t/\tau_S\right]$, τ_S=10ms, and ζ is a random variable uniformly chosen from [0,1). In the simulation, the time step was set at Δt=0.1ms. Activities of presynaptic neurons were generated by rate-modulated Poisson process with $r_i^E(t) = \left[r_X^E + r_S^E s_\mu(t)\right]_+$ for excitatory neuron i modulated by the hidden variable μ. Similarly, the presynaptic inhibitory neuron was described by a Poisson-model with $r^I(t) = \left[r_X^I + r_S^I s_0(t)\right]_+$. Activity of the postsynaptic neuron was given as a Poisson-model with a fixed rate r_{post}. We set parameters $\{r_x^E, r_s^E, r_{post}\}$ in a way that all pre and postsynaptic excitatory neurons show the same firing rate, to avoid the effect of firing-rate difference on synaptic plasticity.

For parameters, we used γ_I=2.0, β_N=1.0, γ_{BP}=8.0, C_p=2.15, y_{th}=250 and other parameters were kept at the same value with the original Schaffer collateral model. Except for Fig. 4D, the delay of inhibitory spike was set as zero. Presynaptic activities were given by r_X^E=1.0Hz, r_S^E=500.0, r_X^I=2.0Hz, r_S^I=1000.0, and postsynaptic firing rate was set as r_{post} = 5.0Hz.

Model A_3: A two-layered single cell model

Previous studies suggest that complicated dendritic computation can be approximated by a two-layered single cell model (Poirazi et al., 2003)(London and Häusser, 2005). Thus, we constructed a single cell model by assuming that each hotspot works as a subunit of a two-layered model. We defined the mean potential of a dendritic subunit *k* by $u_b^k(t) \equiv \sum_{i=1}^{N_b^E} w_i^k u_i^k(t) \big/ \left(w_o^E N_b^E\right)$, and calculated the somatic membrane potential by $u_{soma}(t) \equiv \sum_k g_b\left(u_b^k(t)\right)$. Postsynaptic spikes were given as a rate-modulated Poisson model with the rate $u_{soma}(t)/I_{dv}(t)$. $I_{dv}(t)$ is the divisive inhibition term introduced to keep the output firing rate at r_{post}. By using the mean somatic potential $\frac{d\bar{u}_{soma}(t)}{dt} = -\frac{\bar{u}_{soma}(t)-u_{soma}(t)}{\tau_v}$, $I_{dv}(t)$ was calculated as $I_{dv}(t) \equiv \bar{u}_{soma}(t) \big/ r_{post}$. In the simulation, we used C_p=1.93, τ_v=1s, $g_b(u)=u$ if u>0, otherwise $g_b(u)$=0, and other parameters were kept at the same values with the hotspot model.

Model A$_4$: A model of binocular matching

For the model of critical period plasticity of binocular matching, we used the two-layered single cell model introduced in the previous section (*Model A$_3$*). The neuron has K=100 dendritic branches, each receives $N^E{}_b$=20 excitatory inputs and 1 inhibitory input. At each branch, half of excitatory inputs are from the contralateral eye, and the other half are from the ipsilateral eye. Each excitatory input neuron have direction selectivity characterized with $\theta_{k,i}{}^E$, and shows rate-modulated Poisson firing with

$$r_{k,j}(t) = r_x^E \exp\left[\beta_E \cos\left(\theta(t) - \theta_{k,j}^E\right)\right] \big/ I_0(\beta_E),$$

where $I_0(\beta_E)$ is the modified Bessel function of order 0. Similarly, firing rate of an inhibitory neuron was given as $r_k^I(t) = r_x^I \exp\left[\beta_I \cos\left(\theta(t) - \theta_k^I\right)\right] \big/ I_0(\beta_I)$. For each excitatory input neuron, mean direction selectivity $\{\theta_{k,i}{}^Q\}$ was randomly chosen from a von Mises distribution $\exp\left[\beta_S \cos\left(\theta_{k,i}^Q - \theta_Q\right)\right] \big/ 2\pi I_0(\beta_S)$, where Q={contra, ipsi}. In the simulation, we used θ_{contra}=-π/4, θ_{ipsi}=π/4. Correspondingly, mean direction selectivity of a inhibitory neuron $\{\theta_k{}^I\}$ was defined as the sum of its selectivity for ipsi- and contralateral inputs (ie. $\theta_k{}^I = \theta_k{}^{I,ipsi} + \theta_k{}^{I,contra}$), where $\theta_k{}^{I,ipsi}$ and $\theta_k{}^{I,contra}$ were also randomly depicted from $\exp\left[\beta_S \cos\left(\theta_k^Q - \theta_Q\right)\right] \big/ 2\pi I_0(\beta_S)$. Direction of visual stimulus $\theta(t)$ changes randomly with $\theta(t+\Delta t) = \theta(t) + \sigma_{sr}\zeta_G$ where ζ_G is a Gaussian random variable, and Δt is the time step of the simulation. To mimic monocular deprivation, in the shadowed area of Fig. 7E, we replaced contra-driven input neuron activity with a Poisson spike with constant firing rate $r_{md}{}^E$. In addition, to simulate the lack of contra-driven inputs to inhibitory neurons, we replaced inhibitory activity with $r_k^I(t) = r_{md}^I + \left(r_x^I/2\right)\exp\left[\beta_I \cos\left(\theta(t) - \theta_k^{I,ipsi}\right)\right] \Big/ I_0(\beta_I)$. Similarly, in Fig. 7C, we measured direction selectivity by providing monocular inputs, while replacing the inputs from the other eye with a homogeneous Poisson spikes with firing rate $r_{md}{}^E$.

To evaluate the development of binocular matching, we introduced three order parameters. First, the difference between mean excitatory direction selectivity and inhibitory selectivity at a branch k was evaluated by $\theta_{b,k}^d = \left|\arg\left(\sum_i w_{k,i}^E e^{i\left(\theta_{k,i}^E - \theta_k^I\right)}\right)\right|$. Similarly, the global direction selectivity difference between inputs from the ipsi- and contralateral eyes were defined by

$$\theta_G^d = \hat{d}\left[\arg\left(\sum_{k=1}^{K} \sum_{i \in ipsi} w_{k,i}^E e^{i\theta_{k,i}^E}\right), \arg\left(\sum_{k=1}^{K} \sum_{i \in contra} w_{k,i}^E e^{i\theta_{k,i}^E}\right)\right],$$

where the function $\hat{d}[\theta_1, \theta_2]$ calculates the phase difference between two angles. Finally, direction selectivity index DSI for binocular input was calculated by

$$DSI = \left|\sum_{k=1}^{K} \sum_{i=1}^{N_b^E} w_{k,i}^E e^{i\theta_{k,i}^E} \Big/ \sum_{k=1}^{K} \sum_{i=1}^{N_b^E} w_{k,i}^E\right|.$$

For the calculation of the monocular direction selectivity index, at each branch k, we took sum over $N_b{}^E/2$ excitatory inputs corresponding to the each eye instead of all $N_b{}^E$ inputs.

In the simulation, we set γ_I=2.5, C_p=1.85, y_{th}=750.0, and the rest of parameters were kept at the values used in the *Model A*$_3$. Inputs parameters were set at β_E=4.0, β_I=2.0, β_S=1.0, θ_{contra}=-π/4, θ_{ipsi}=π/4, $r_X{}^E$=5.0, $r_X{}^I$=10.0, $r_{md}{}^E$=1.0, $r_{md}{}^I$=1.0, $\sigma_{sr} = 0.1\sqrt{\Delta t}$.

Model B: A reduced analytical model of a spine

If we shrink equations for membrane potential and calcium concentration into one, the reduced equation would be written as,

$$\begin{aligned}\frac{dC_i(t)}{dt} = &-\frac{C_i(t)}{\tau_C} + C_{pre}X_i(t) + C_{post}\left[1 + g_C\left(C_i(t-\Delta t)\right)\right]X_{post}(t)\\ &-C_I \sum_{j \in \Omega_i^I} X_j^I(t - d_I) + C_E \sum_{j \in \Omega_i^E} X_j^E(t - d_E),\end{aligned}$$

where $g_c(X) = \eta[X]_+$ captures the nonlinear effect caused by pre-post coincidence. g_c was calculated from the value of C_i at t=t-Δt to avoid pathological divergence caused by the delta function. In the simulation, we simply used value of C_i one time step before. Here, all input X_i, X_{post}, $X_j{}^I$, $X_j{}^E$ are given as point processes, and d_I, d_E are heterosynaptic delays. For the intermediate y, we used the same equation as before. Note that above equation is basically same with the one in (Graupner and Brunel, 2012) except for the nonlinear term $g_c(C)$ and the heterosynaptic terms.

Let us consider weight dynamics of an excitatory synapse that has only one inhibitory synapse in its neighbor. For analytical tractability, we consider the case when presynaptic, postsynaptic, and inhibitory neurons fire only one spikes at t=t_{pre}, t_{post}, t_I respectively. In case of the CA1 experiment, because GABA uncaging was always performed before pre and postsynaptic spike, the timing of inhibitory spike is given as $t_I = \min(t_{pre}, t_{post}) - \delta_I$ for $\delta_I > 0$. Note that spike timings are counted at the excitatory spine, so the actual timings are $t'_{pre}=t_{pre}-d_{axon}$, $t'_{post}=t_{post}-d_{dendrite}$, $t'_I= t_I-d_I-d_{inh\_axon}$. In this setting, the change in intermediate variable of the excitatory synapse is given as

$$\Delta y = \begin{cases} G_1\left(C_1, t_{pre}-t_{post}\right) + G_2\left(C_{pre} + C_1 e^{-\left(t_{pre}-t_{post}\right)/\tau_C}\right) & (\text{if } \ t_{post} < t_{pre}) \\ G_1\left(C_2, t_{post}-t_{pre}\right) + G_2\left(C_{post}\left[1 + g_C\left(C_2 e^{-\left(t_{post}-t_{pre}\right)/\tau_C}\right)\right] + C_2 e^{-\left(t_{post}-t_{pre}\right)/\tau_C}\right) & (\text{otherwise}) \end{cases}$$

where,

$$C_1 \equiv C_{post} - C_I e^{-\left(t_{post}-t_I\right)/\tau_C}, \quad C_2 \equiv C_{pre} - C_I e^{-\left(t_{pre}-t_I\right)/\tau_C}$$

$$\begin{aligned} G_1(C,\Delta t) \equiv B_p\left[C-\theta_p\right]_+ &\left(\left[\tau_C \log\tfrac{C}{\theta_p} - \Delta t\right]_+ \Delta t + \left[\Delta t - \tau_C \log\tfrac{C}{\theta_p}\right]_+ \tau_C \log\tfrac{C}{\theta_p}\right) \\ -B_d\left[C-\theta_d\right]_+ &\left(\left[\tau_C \log\tfrac{C}{\theta_d} - \Delta t\right]_+ \Delta t + \left[\Delta t - \tau_C \log\tfrac{C}{\theta_d}\right]_+ \tau_C \log\tfrac{C}{\theta_d}\right), \end{aligned}$$

$$G_2(C) \equiv B_p\left[C-\theta_p\right]_+ \tau_C \log\tfrac{C}{\theta_p} - B_d\left[C-\theta_d\right]_+ \tau_C \log\tfrac{C}{\theta_d}.$$

Similarly, in case of the striatum experiment, by setting η=0, the change in the intermediate variable is given as

$$\Delta y = \begin{cases} G_1\left(C_{post}, t_{pre}-t_{post}\right) + G_1\left(C_3, t_I - t_{pre}\right) + G_2\left(-C_I + C_3 e^{-\left(t_I-t_{pre}\right)/\tau_C}\right) & (\text{if } \ t_{post} < t_{pre} < t_I) \\ G_1\left(C_{pre}, t_I - t_{pre}\right) + G_1\left(C_4, t_{post} - t_I\right) + G_2\left(C_{post} + C_4 e^{-\left(t_{post}-t_I\right)/\tau_C}\right) & (\text{if } \ t_{pre} < t_I < t_{post}) \\ G_1\left(C_{pre}, t_{post}-t_{pre}\right) + G_1\left(C_5, t_I - t_{post}\right) + G_2\left(-C_I + C_5 e^{-\left(t_I-t_{post}\right)/\tau_C}\right) & (\text{if } \ t_{pre} < t_{post} < t_I), \end{cases}$$

where

$$C_3 \equiv C_{pre} + C_{post} e^{-\left(t_{pre}-t_{post}\right)/\tau_C}, \quad C_4 \equiv -C_I + C_{pre} e^{-\left(t_I-t_{pre}\right)/\tau_C}, \text{ and } \ C_5 \equiv C_{post} + C_{pre} e^{-\left(t_{post}-t_{pre}\right)/\tau_C}.$$

In the simulation, parameters were set at τ_c=30ms, C_{post}=2.0, θ_p=1.6, θ_d=1.0, B_p=2.25, B_d=1.0. Additionally, in the model of a Schaffer collateral synapse, we used δ_I=1.0, C_{pre}=1.0, C_E=0.30, η=2.0, and for the model of a cortico-striatal synapse, we employed δ_I=5.0, C_{pre}=0.75, C_E=0.0, η=0.0.

In Fig. 3C and D, we used the parameter set for the model of Schaffer collateral synapse.

Model C: Detailed single NEURON model

To see whether the dendritic E/I balance indeed benefits single neuron computation, we studied dendritic computation in detailed single neuron models using NEURON simulator (Hines and Carnevale, 1997). For the morphology and active properties of the neuron, we employed a previously developed model of spiny neuron in cortical layer 4 (Mainen and Sejnowski, 1996). On the model, we distributed synaptic inputs in three different ways, and studied their response for stochastic stimuli from five independent sources.

First, in all three models, we uniformly distributed 200 inhibitory inputs on every 28 μm of the dendritic tree (Fig. 6A left). The inputs are selective for one of five stimuli, as indicated by colors in Figure 6A-left, and none of inhibitory inputs are spatially clustered. Synaptic inputs were approximated with double exponential conductance change, where rise and decay time constants were 0.1ms and 10ms respectively, and the reversal potential was set at -70mV. For the activity, we assumed that each presynaptic inhibitory neuron responds to its selective stimuli with a homogeneous Poisson firing, and stays silent otherwise. Here, we assumed 5 milliseconds delay between excitatory and inhibitory inputs.

Based on the given distribution of inhibitory inputs, in the dendritic E/I balance model, we distributed excitatory inputs in a way that selectivity of excitatory and inhibitory inputs matches locally. To this end, of 1000 excitatory inputs placed at every 5.5μm, we assumed that five neighboring inputs show the same selectivity, so that the selectivity of each excitatory input roughly matches the selectivity of the nearest inhibitory input (Fig. 6A middle-left). As we have shown in Figure 4 and 5, this input distribution can be achieved through heterosynaptic plasticity, even if initially excitatory selectivity is random distributed. As for synaptic inputs, we modeled both AMPA and NMDA channels by considering two synapse models with different timescales. For AMPA inputs, rise and decay time constants were set at 0.1ms and 5.0ms, whereas in NMDA inputs rise and decay time constants were 1.0ms and 50ms. In both channels, the reversal potential was set at 0mV. The activity was modeled as a homogeneous Poisson spiking during the selective stimuli, and total silence otherwise.

To perform comparison, we considered two additional excitatory inputs distributions. One is a random model, in which excitatory selectivity do not have any clustering structure (Fig. 6A middle-right). The other one is excitatory clustering model, in which five neighboring excitatory inputs have the same selectivity as in the dendritic E/I balance model, but the selectivity of the cluster is different from the selectivity of nearest inhibitory inputs (Fig. 6A-right). Excitatory clustering model was created by misaligning the excitatory inputs in the dendritic E/I balance model. In both models, synapses and activity were modeled in the same way with the dendritic E/I balance model.

In the simulations, duration of each stimulus was uniformly sampled from 300-700ms. The ratio of change detecting spikes was calculated by

$$ratio = \frac{\sum_k \sum_{\mu=2}^{5} \left[0 \le s_k - t_\mu^s \le 25\text{ms} \right]_+}{\sum_k \left[t_2^s \le s_k \le t_5^f \right]_+}$$

where $\{s_k\}$ are timings of output spikes, $t_\mu{}^s$ and $t_\mu{}^f$ are the starting point and the end point of the μ-th stimulus. We excluded the first stimulus (μ=1) from the evaluation, because the model often exhibited bursty activity regardless of synaptic configuration. The data points in Fig. 6C,D was calculated by averaging over 100 simulations. Parameter settings and additional details of the model will be available at the modelDB.

Acknowledgments

The authors thank to Dr. Laurent Venance for kindly providing the experimental data. This work was partly supported by JSPS Doctorial Fellowship DC2 (NH), and KAKENHI No15H04625 (TF).

Competing interests

The authors have declared that no competing interests exist.

References

Bar-Ilan, L., Gidon, A., Segev, I., 2013. The role of dendritic inhibition in shaping the plasticity of excitatory synapses. Front. Neural Circuits 6. doi:10.3389/fncir.2012.00118

Bazelot, M., Bocchio, M., Kasugai, Y., Fischer, D., Dodson, P.D., Ferraguti, F., Capogna, M., 2015. Hippocampal Theta Input to the Amygdala Shapes Feedforward Inhibition to Gate Heterosynaptic Plasticity. Neuron 87, 1290–1303. doi:10.1016/j.neuron.2015.08.024

Bi, G.Q., Poo, M.M., 1998. Synaptic modifications in cultured hippocampal neurons: dependence on spike timing, synaptic strength, and postsynaptic cell type. J. Neurosci. Off. J. Soc. Neurosci. 18, 10464–10472.

Blaise, J.H., Bronzino, J.D., 2003. Effects of stimulus frequency and age on bidirectional synaptic plasticity in the dentate gyrus of freely moving rats. Exp. Neurol. 182, 497–506. doi:10.1016/S0014-4886(03)00136-5

Branco, T., Clark, B.A., Häusser, M., 2010. Dendritic Discrimination of Temporal Input Sequences in Cortical Neurons. Science 329, 1671–1675. doi:10.1126/science.1189664

Caporale, N., Dan, Y., 2008. Spike Timing–Dependent Plasticity: A Hebbian Learning Rule. Annu. Rev. Neurosci. 31, 25–46. doi:10.1146/annurev.neuro.31.060407.125639

Chen, J.-Y., Lonjers, P., Lee, C., Chistiakova, M., Volgushev, M., Bazhenov, M., 2013. Heterosynaptic Plasticity Prevents Runaway Synaptic Dynamics. J. Neurosci. 33, 15915–15929. doi:10.1523/JNEUROSCI.5088-12.2013

Chen, X., Leischner, U., Rochefort, N.L., Nelken, I., Konnerth, A., 2011. Functional mapping of single spines in cortical neurons in vivo. Nature 475, 501–505. doi:10.1038/nature10193

Cutsuridis, V., 2011. GABA inhibition modulates NMDA-R mediated spike timing dependent plasticity (STDP) in a biophysical model. Neural Netw. 24, 29–42. doi:10.1016/j.neunet.2010.08.005

Dorrn, A.L., Yuan, K., Barker, A.J., Schreiner, C.E., Froemke, R.C., 2010. Developmental sensory experience balances cortical excitation and inhibition. Nature 465, 932–936. doi:10.1038/nature09119

Espinosa, J.S., Stryker, M.P., 2012. Development and Plasticity of the Primary Visual Cortex. Neuron 75, 230–249. doi:10.1016/j.neuron.2012.06.009

Froemke, R.C., 2015. Plasticity of Cortical Excitatory-Inhibitory Balance. Annu. Rev. Neurosci. 38, 195–219. doi:10.1146/annurev-neuro-071714-034002

Gambino, F., Pagès, S., Kehayas, V., Baptista, D., Tatti, R., Carleton, A., Holtmaat, A., 2014. Sensory-evoked LTP driven by dendritic plateau potentials in vivo. Nature 515, 116–119. doi:10.1038/nature13664

Gerstner, W., Kempter, R., van Hemmen, J.L., Wagner, H., 1996. A neuronal learning rule for sub-millisecond temporal coding. Nature 383, 76–81. doi:10.1038/383076a0

Gidon, A., Segev, I., 2012. Principles Governing the Operation of Synaptic Inhibition in Dendrites. Neuron 75, 330–341. doi:10.1016/j.neuron.2012.05.015

Graupner, M., Brunel, N., 2012. Calcium-based plasticity model explains sensitivity of synaptic changes to spike pattern, rate, and dendritic location. Proc. Natl. Acad. Sci. 109, 3991–3996. doi:10.1073/pnas.1109359109

Graupner, M., Brunel, N., 2007. STDP in a Bistable Synapse Model Based on CaMKII and Associated Signaling Pathways. PLoS Comput Biol 3, e221. doi:10.1371/journal.pcbi.0030221

Harvey, C.D., Svoboda, K., 2007. Locally dynamic synaptic learning rules in pyramidal neuron dendrites. Nature 450, 1195–1200. doi:10.1038/nature06416

Hayama, T., Noguchi, J., Watanabe, S., Takahashi, N., Hayashi-Takagi, A., Ellis-Davies, G.C.R., Matsuzaki, M., Kasai, H., 2013. GABA promotes the competitive selection of dendritic spines by controlling local Ca2+ signaling. Nat. Neurosci. 16, 1409–1416. doi:10.1038/nn.3496

Hensch, T.K., 2005. Critical period plasticity in local cortical circuits. Nat. Rev. Neurosci. 6, 877–888. doi:10.1038/nrn1787

Higley, M.J., Sabatini, B.L., 2012. Calcium Signaling in Dendritic Spines. Cold Spring Harb. Perspect. Biol. 4, a005686. doi:10.1101/cshperspect.a005686

Hines, M.L., Carnevale, N.T., 1997. The NEURON Simulation Environment. Neural Comput. 9, 1179–1209. doi:10.1162/neco.1997.9.6.1179

Hiratani, N., Fukai, T., 2015. Mixed Signal Learning by Spike Correlation Propagation in Feedback Inhibitory Circuits. PLoS Comput Biol 11, e1004227. doi:10.1371/journal.pcbi.1004227

Jedlicka, P., Benuskova, L., Abraham, W.C., 2015. A Voltage-Based STDP Rule Combined with Fast BCM-Like Metaplasticity Accounts for LTP and Concurrent “Heterosynaptic” LTD in the Dentate Gyrus In Vivo. PLOS Comput Biol 11, e1004588. doi:10.1371/journal.pcbi.1004588

Jia, H., Rochefort, N.L., Chen, X., Konnerth, A., 2010. Dendritic organization of sensory input to cortical neurons in vivo. Nature 464, 1307–1312. doi:10.1038/nature08947

Kleindienst, T., Winnubst, J., Roth-Alpermann, C., Bonhoeffer, T., Lohmann, C., 2011. Activity-Dependent Clustering of Functional Synaptic Inputs on Developing Hippocampal Dendrites. Neuron 72, 1012–1024. doi:10.1016/j.neuron.2011.10.015

Koch, C., 1998. Biophysics of Computation: Information Processing in Single Neurons. Oxford University Press.

Kremkow, J., Aertsen, A., Kumar, A., 2010. Gating of Signal Propagation in Spiking Neural Networks by Balanced and Correlated Excitation and Inhibition. J. Neurosci. 30, 15760–15768. doi:10.1523/JNEUROSCI.3874-10.2010

Kuhlman, S.J., Tring, E., Trachtenberg, J.T., 2011. Fast-spiking interneurons have an initial orientation bias that is lost with vision. Nat. Neurosci. 14, 1121–1123. doi:10.1038/nn.2890

Liu, G., 2004. Local structural balance and functional interaction of excitatory and inhibitory synapses in hippocampal dendrites. Nat. Neurosci. 7, 373–379. doi:10.1038/nn1206

London, M., Häusser, M., 2005. Dendritic Computation. Annu. Rev. Neurosci. 28, 503–532. doi:10.1146/annurev.neuro.28.061604.135703

Lüscher, C., Malenka, R.C., 2012. NMDA Receptor-Dependent Long-Term Potentiation and Long-Term Depression (LTP/LTD). Cold Spring Harb. Perspect. Biol. 4, a005710. doi:10.1101/cshperspect.a005710

Mainen, Z.F., Sejnowski, T.J., 1996. Influence of dendritic structure on firing pattern in model neocortical neurons. Nature 382, 363–366. doi:10.1038/382363a0

Malenka, R.C., Bear, M.F., 2004. LTP and LTD: An Embarrassment of Riches. Neuron 44, 5–21. doi:10.1016/j.neuron.2004.09.012

Markram, H., Toledo-Rodriguez, M., Wang, Y., Gupta, A., Silberberg, G., Wu, C., 2004. Interneurons of the neocortical inhibitory system. Nat. Rev. Neurosci. 5, 793–807. doi:10.1038/nrn1519

Ma, W., Liu, B., Li, Y., Huang, Z.J., Zhang, L.I., Tao, H.W., 2010. Visual Representations by Cortical Somatostatin Inhibitory Neurons—Selective But with Weak and Delayed Responses. J. Neurosci. 30, 14371–14379. doi:10.1523/JNEUROSCI.3248-10.2010

Mel, B.W., Schiller, J., 2004. On the Fight Between Excitation and Inhibition: Location Is Everything. Sci. Signal. 2004, pe44–pe44. doi:10.1126/stke.2502004pe44

Moore, A.K., Wehr, M., 2013. Parvalbumin-Expressing Inhibitory Interneurons in Auditory Cortex Are Well-Tuned for Frequency. J. Neurosci. 33, 13713–13723. doi:10.1523/JNEUROSCI.0663-13.2013

Müllner, F.E., Wierenga, C.J., Bonhoeffer, T., 2015. Precision of Inhibition: Dendritic Inhibition by Individual GABAergic Synapses on Hippocampal Pyramidal Cells Is Confined in Space and Time. Neuron 87, 576–589. doi:10.1016/j.neuron.2015.07.003

Nishiyama, J., Yasuda, R., 2015. Biochemical Computation for Spine Structural Plasticity. Neuron 87, 63–75. doi:10.1016/j.neuron.2015.05.043

Oh, W.C., Parajuli, L.K., Zito, K., 2015. Heterosynaptic Structural Plasticity on Local Dendritic Segments of Hippocampal CA1 Neurons. Cell Rep. 10, 162–169. doi:10.1016/j.celrep.2014.12.016

Paille, V., Fino, E., Du, K., Morera-Herreras, T., Perez, S., Kotaleski, J.H., Venance, L., 2013. GABAergic Circuits Control Spike-Timing-Dependent Plasticity. J. Neurosci. 33, 9353–9363. doi:10.1523/JNEUROSCI.5796-12.2013

Petersen, C.C.H., Malenka, R.C., Nicoll, R.A., Hopfield, J.J., 1998. All-or-none potentiation at CA3-CA1 synapses. Proc. Natl. Acad. Sci. 95, 4732–4737.

Poirazi, P., Brannon, T., Mel, B.W., 2003. Pyramidal Neuron as Two-Layer Neural Network. Neuron 37, 989–999. doi:10.1016/S0896-6273(03)00149-1

Santamaria, F., Wils, S., De Schutter, E., Augustine, G.J., 2006. Anomalous Diffusion in Purkinje Cell Dendrites Caused by Spines. Neuron 52, 635–648. doi:10.1016/j.neuron.2006.10.025

Shouval, H.Z., Bear, M.F., Cooper, L.N., 2002. A unified model of NMDA receptor-dependent bidirectional synaptic plasticity. Proc. Natl. Acad. Sci. 99, 10831–10836. doi:10.1073/pnas.152343099

Song, S., Miller, K.D., Abbott, L.F., 2000. Competitive Hebbian learning through spike-timing-dependent synaptic plasticity. Nat. Neurosci. 3, 919–926. doi:10.1038/78829

Takahashi, N., Kitamura, K., Matsuo, N., Mayford, M., Kano, M., Matsuki, N., Ikegaya, Y., 2012. Locally Synchronized Synaptic Inputs. Science 335, 353–356. doi:10.1126/science.1210362

Takesian, A.E., Hensch, T.K., 2013. Balancing plasticity/stability across brain development. Prog. Brain Res. 207, 3–34. doi:10.1016/B978-0-444-63327-9.00001-1

Tsukada, M., Aihara, T., Kobayashi, Y., Shimazaki, H., 2005. Spatial analysis of spike-timing-dependent LTP and LTD in the CA1 area of hippocampal slices using optical imaging. Hippocampus 15, 104–109. doi:10.1002/hipo.20035

Vogels, T.P., Sprekeler, H., Zenke, F., Clopath, C., Gerstner, W., 2011. Inhibitory Plasticity Balances Excitation and Inhibition in Sensory Pathways and Memory Networks. Science 334, 1569–1573. doi:10.1126/science.1211095

Wang, B.-S., Feng, L., Liu, M., Liu, X., Cang, J., 2013. Environmental Enrichment Rescues Binocular Matching of Orientation Preference in Mice that Have a Precocious Critical Period. Neuron 80, 198–209. doi:10.1016/j.neuron.2013.07.023

Wang, B.-S., Sarnaik, R., Cang, J., 2010. Critical Period Plasticity Matches Binocular Orientation Preference in the Visual Cortex. Neuron 65, 246–256. doi:10.1016/j.neuron.2010.01.002

Wilson, N.R., Ty, M.T., Ingber, D.E., Sur, M., Liu, G., 2007. Synaptic Reorganization in Scaled Networks of Controlled Size. J. Neurosci. 27, 13581–13589. doi:10.1523/JNEUROSCI.3863-07.2007

Yazaki-Sugiyama, Y., Kang, S., Câteau, H., Fukai, T., Hensch, T.K., 2009. Bidirectional plasticity in fast-spiking GABA circuits by visual experience. Nature 462, 218–221. doi:10.1038/nature08485

Zenke, F., Agnes, E.J., Gerstner, W., 2015. Diverse synaptic plasticity mechanisms orchestrated to form and retrieve memories in spiking neural networks. Nat. Commun. 6. doi:10.1038/ncomms7922

Table 1. Definitions of variables

$u_i(t)$	Membrane potential at spine *i*	Eq. 2
$c_i(t)$	Calcium concentration at spine *i*	Eq. 3
$y_i(t)$	Intermediate factor (interim synaptic weight)	Eq. 5
$w_i(t)$	Synaptic weight of spine *i*	Eq. 6
$g_N(u)$	Voltage dependence of NMDA receptor	$g_N(u_i)=\alpha_N u_i+\beta_N$
$g_V(u)$	Voltage dependence of VDCC	$g_v(u_i)=\alpha_v u_i$
$x^A{}_i(t)$	Inputs through AMPA receptor	Eq. 4 (Q=A)
$x^N{}_i(t)$	Inputs through NMDA receptor	Eq. 4 (Q=N)
$x^{BP}{}_i(t)$	Back propagation	Eq. 4 (Q=BP)
$x^E{}_i(t)$	Excitatory heterosynaptic inputs	Eq. 4 (Q=E)
$x^I{}_i(t)$	Inhibitory heterosynaptic inputs	Eq. 4 (Q=I)
$u_b{}^k(t)$	Membrane potential at dendritic branch *k*	$u_b^k(t)=\sum_{i=1}^{N_b^E} w_i^k u_i^k(t) \Big/ \left(w_o^E N_b^E\right)$
$u_{soma}(t)$	Membrane potential at the soma	$u_{soma}(t)=\sum_k g_b\left(u_b^k(t)\right)$
$g_b(u)$	Dendritic nonlinearity function	$g_b(u)=\begin{cases} u & (\text{if } u>0) \\ 0 & (\text{otherwise}) \end{cases}$

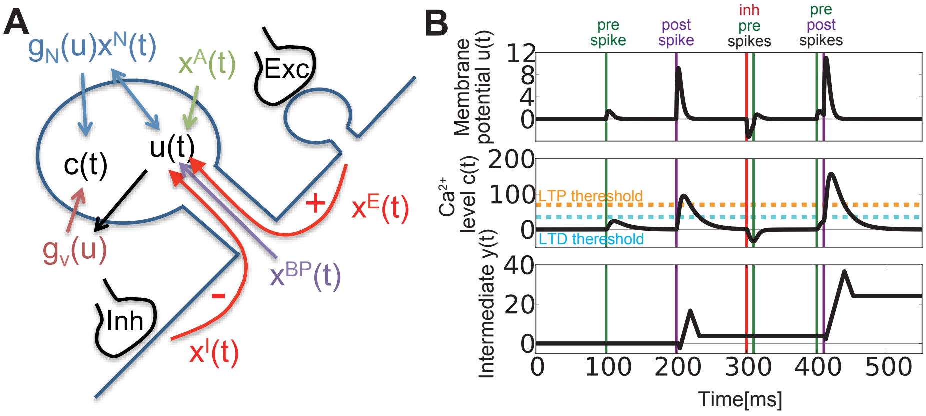
A
$g_N(u)x^N(t)$
$x^A(t)$
Exc
c(t)
u(t)
$g_v(u)$
+
$x^E(t)$
$x^{BP}(t)$
-
Inh
$x^I(t)$
B
pre spike
post spike
inh pre spikes
pre post spikes
Membrane potential u(t)
12
8
4
0
Ca^{2+} level c(t)
200
100
0
LTP threshold
LTD threshold
Intermediate y(t)
40
20
0
0
100
200
300
400
500
Time[ms]

Figure 1: **Schematic figure of the model of heterosynaptic spike-timing-dependent plasticity (h-STDP). A**) Two variables in the spine $u(t)$ and $c(t)$ represent the normalized membrane potential and Ca^{2+} concentration respectively. Presynaptic action potentials modulate the membrane potential $u(t)$ through AMPA (x^A) and NMDA ($g_N(u)x^N$) receptors. In addition, $u(t)$ is modified by back-propagation (x^{BP}), and heterosynaptic current caused by excitatory (x^E) and inhibitory (x^I) inputs. Calcium level $c(t)$ is modulated by influx/outflux through NMDA ($g_N(u)x^N$) and VDCC ($g_V(u)$). Consequently, $c(t)$ is indirectly controlled by $u(t)$ because both NMDA and VDCC are voltage-dependent. **B**) An example of dynamics of the membrane potential variable $u(t)$ (top), Ca^{2+} concentration $c(t)$ (middle), and the intermediate variable $y(t)$ that controls the synaptic weight $w(t)$(bottom). Change in the Ca^{2+} level roughly follows the membrane potential dynamics, and the intermediate variable $y(t)$ is positively (negatively) modulated when Ca^{2+} level is above LTP(LTD) thresholds represented by orange(cyan) dotted lines. Based on the intermediate variable $y(t)$, synaptic weight $w(t)$ is updated in a slow timescale (see Fig. **4C** for example).

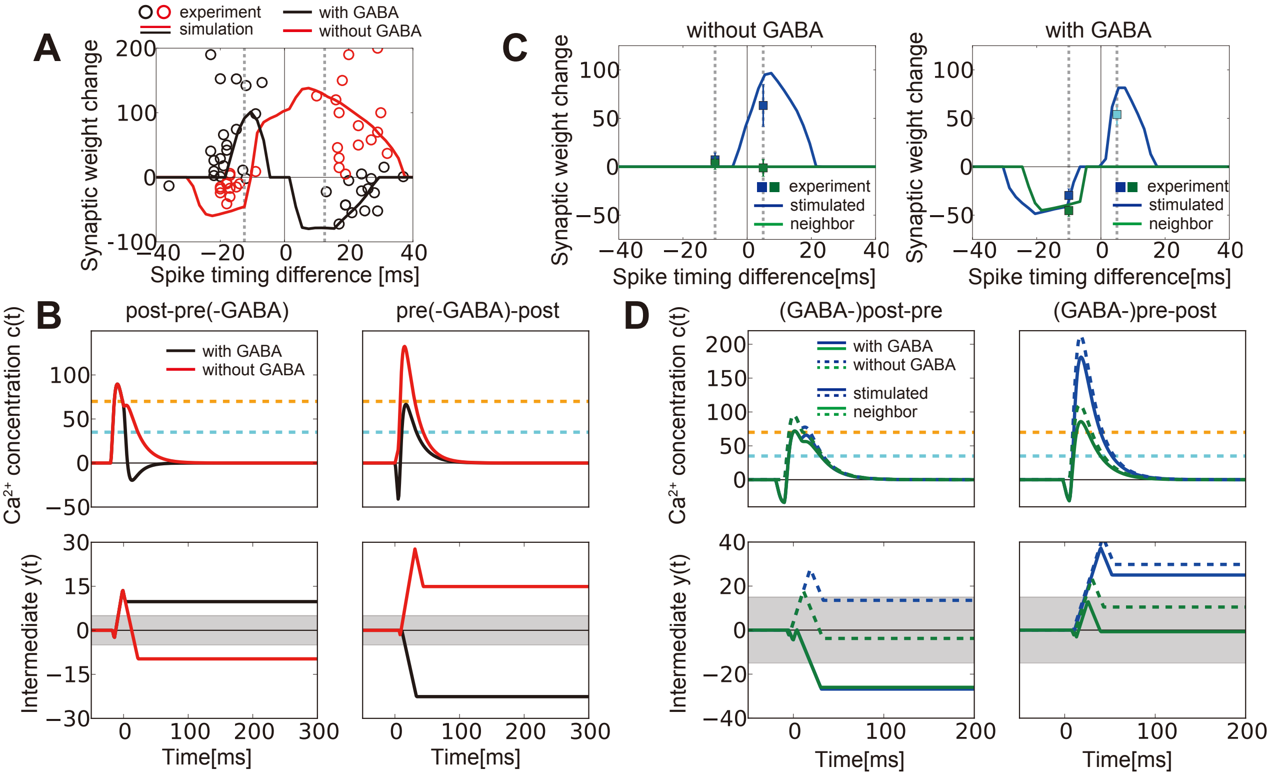

Figure 2: **The model reproduces spike-timing-dependent heterosynaptic effects. A**) Spike timing window with/without a di-synaptic GABAergic input. Lines are simulation data, and points are experimental data taken from (Paille et al., 2013). Vertical dotted lines represent the spike-timing differences at which Fig. **B** is calculated. **B**) Dynamics of calcium concentration $c(t)$ (top) and the intermediate variable $y(t)$ (bottom) at the stimulated spine. Gray areas in the bottom figures represent regions satisfying $y(t) < y_{th}/K_{rep}$, in which the change in the intermediate is not reflected into synaptic weight, where K_{rep} represents the number of paired stimulation given in the simulation for Fig. **A**. **C**) Synaptic weight change with/without GABAergic inputs right before pre/post stimulation. Data points were taken from (Hayama et al., 2013). The cyan point is a result from muscimol application, not GABA uncaging. **D**) Dynamics of $c(t)$ and $y(t)$ at the stimulated spine (blue lines) and a neighboring spine (green lines).

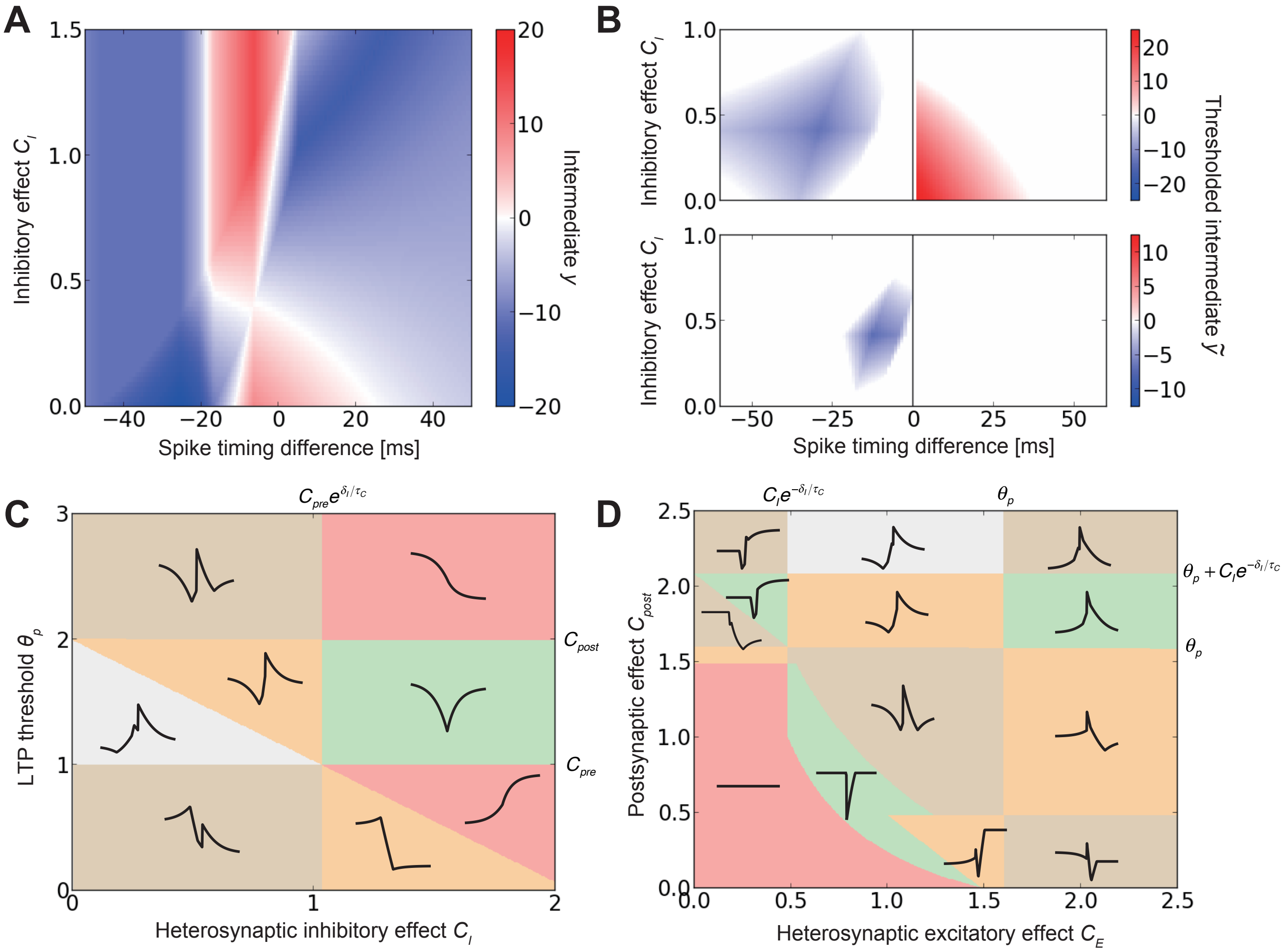

Figure 3: **Heterosynaptic STDP can be understood as phase transitions on STDP time window in an analytical model. A, B**) STDP windows at various strength of heterosynaptic inhibitory effect C_I. Fig. **A** corresponds to the striatum experiment, and Fig. **B** corresponds to the CA1 experiment. Note that values in Fig. **B** were calculated by $\tilde{y} = \mathrm{sgn}(y) \cdot [y - 15]_+$ to reflect the effect of thresholding. **C**) Phase diagram of STDP time window calculated for inhibitory effect C_I and LTP threshold θ_p. Colors show the number of local minimum/maximum, and lines are typical STDP time windows at each phase. Parameters written on right-side (top) of the panel represent the critical values of θ_p (C_I). **D**) Phase diagram calculated for heterosynaptic excitatory effect parameter C_E and postsynaptic effect parameters C_{post} at a fixed inhibitory effect ($C_I = 0.5$).

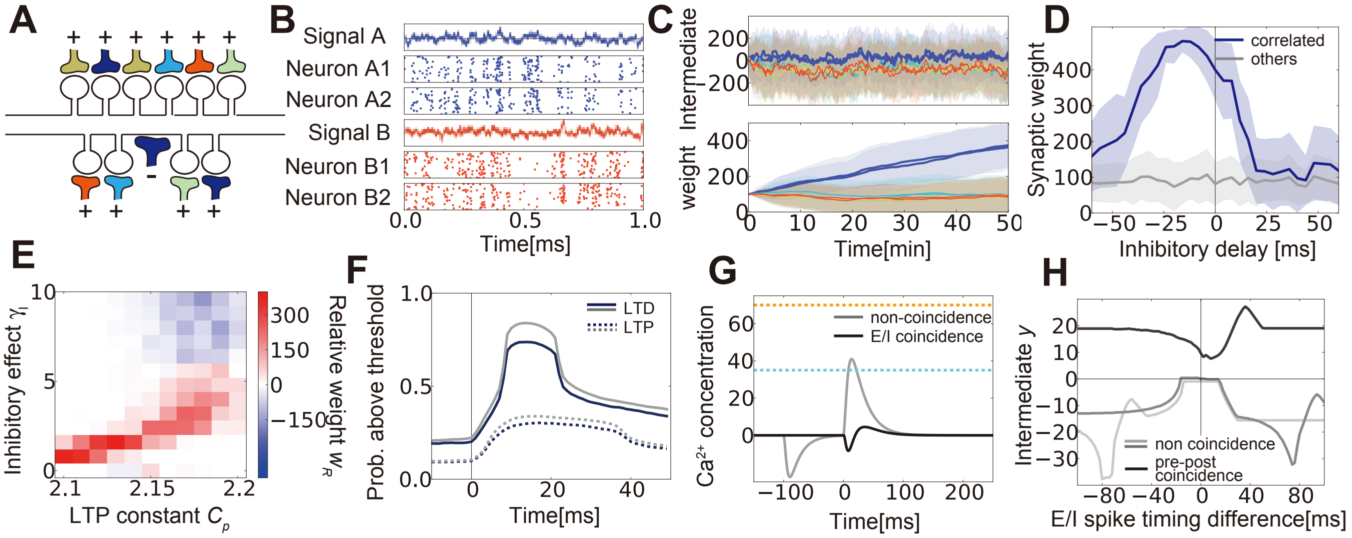

Figure 4: **Emergence of detailed dendritic excitatory/inhibitory balance by heterosynaptic STDP.** **A**) A schematic figure of a dendritic hotspot model. The shaft synapse represent an inhibitory input. Colors represent spike correlation between synaptic inputs. **B**) Examples of correlated spike inputs. Each raster plot was calculated from 50 simulation trials. **C**) Changes in intermediate variable y(top) and weight w(bottom) by h-STDP. The blue lines represent dynamics of synapses correlated with the inhibitory input. **D**) Synaptic weight change at the excitatory synapses correlated with the inhibitory inputs, at various inhibitory delays. Error bars in Fig. **C** and **D** represent standard deviations over 50 simulation trials. **E**) Relative weight changes w_R calculated at various parameters. We defined w_R by $\langle w_i^E \rangle_{i \in \text{corr}} - \langle w_i^E \rangle_{i \in \text{un-corr}}$, where "corr" represents a set of excitatory synapses correlated with the inhibitory synapse, and "un-corr" stands for uncorrelated ones. Here, weights were calculated by taking average over 10 simulations. **F**) Probability of LTP/LTD occurrence calculated from a simulation. Lines represent the mean LTP/LTD probabilities at excitatory synapses correlated with the inhibitory input (blue lines) and other synapses (gray lines), respectively. **G, H**) Results in single-spike simulations. E/I coincidence prevents LTD effect due to pre-spike (**G**), without affecting LTP effect due to pre-post coincidence (**H**). In Fig. **G**, inhibitory spikes were provided at $t = 0$ in the black line, $t = -100$ms in the gray line, and the excitatory presynaptic spike was given at $t = 0$ in both lines. Similarly, in Fig. **H**, postsynaptic spikes were provided at $t = -75$ (light-gray), 0 (black), +75ms (dark-gray), and the presynaptic spike was given at $t = 0$ in all lines.

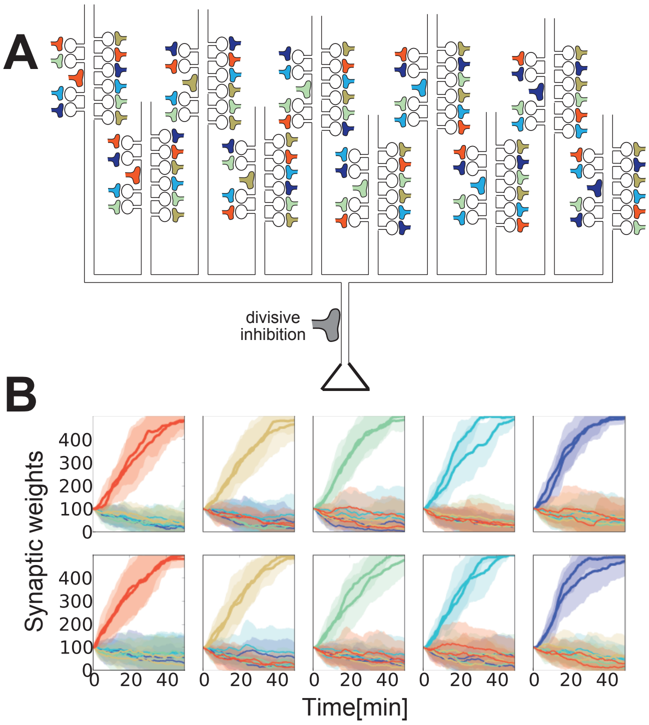

Figure 5: **Detailed dendritic excitatory/inhibitory balance in a two-layered single cell model.** **A**) Schematics of the single cell model. In the model, each branch receives 10 excitatory inputs and 1 inhibitory input. As in Fig. **4A**, inhibitory inputs are represented by shaft synapses. The left (right) branch corresponds to the bottom-left (top-right) branch in Fig. **B**. **B**) Synaptic weight change at each branch. Error bars are standard deviations over 10 simulation trials.

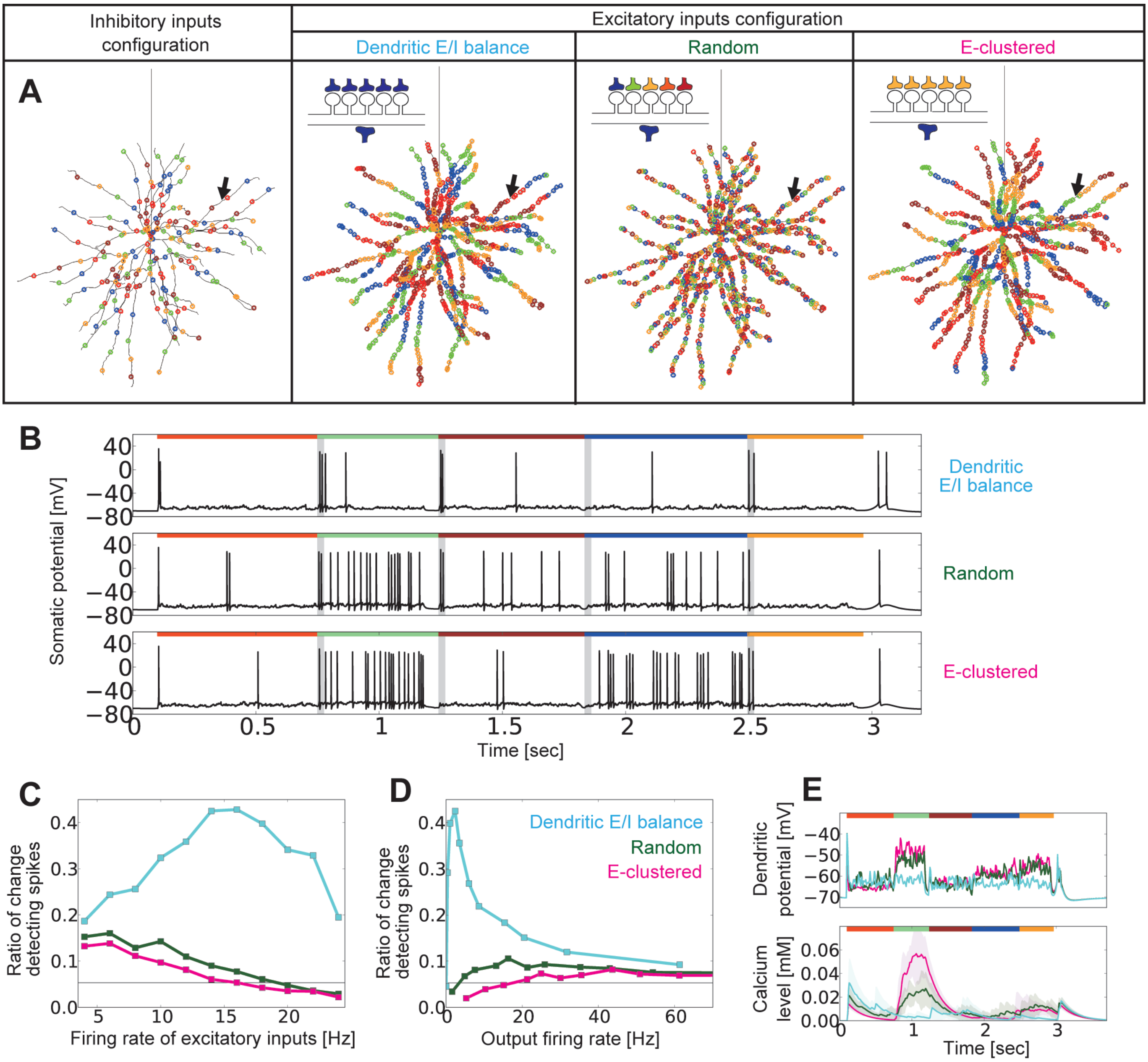

Figure 6: **Dendritic excitatory/inhibitory balance enables change detection in a detailed single neuron model. A**) Synaptic organization in the model. Colored points on the dendrites indicate sites of synaptic inputs, and the color represents the type of stimulus for which its presynaptic neuron is selective (see Model C in Method for details). The vertical lines represent the axon, and the arrows indicate the point at which the data for Fig. **E** was recorded. Schematic figures at the left top of neurons describe the ways selectivity of excitatory synapses was configured. In the schematic figures, shaft synapses represent inhibitory synaptic inputs, and spine synapses represent nearby excitatory inputs. **B**) Examples of neural response for five continuous stimuli in the three models. Colored horizontal bars at the top of panels represent the type of stimulus presented, and the gray vertical bars represent the change points. **C, D**) Ratio of change detecting spikes in three models. In Fig. **C**, we modified firing rates of both excitatory and inhibitory inputs, while keeping their ratio at $r_I = 4r_E$. In Fig. **D**, we modified the firing rate of inhibitory inputs, while fixing the firing rate of excitatory inputs at 14Hz. Horizontal black lines represent the chance level. **E**) Traces of dendritic membrane potential (top) and intracellular calcium concentration (bottom) at the dendrite pointed by the arrow in Fig. **A**, for the stimulus configuration depicted in Fig. **B**.

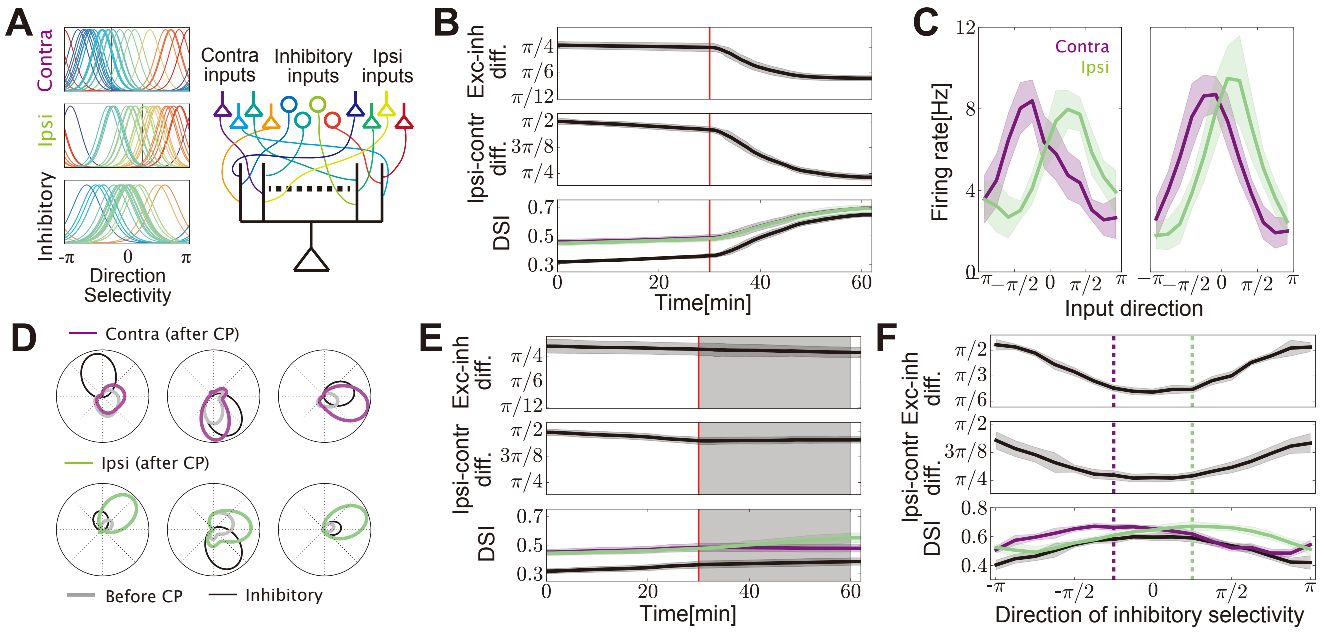

Figure 7: **Heterosynaptic plasticity can trigger binocular matching. A**) (left) Direction selectivity of input neurons. In the model, as depicted by black vertical lines, majorities of excitatory input neurons from the contralateral (ipsilateral) eye are selective for directions around $\theta = -\pi/4$ ($\theta = \pi/4$), while inputs from the inhibitory neurons are weakly selective for $\theta = 0$. (right) A schematic figure of model configuration. Each dendritic branch receives inputs from both ipsi- and contralateral driven excitatory neurons and also from inhibitory neurons. **B**) (top): Difference between mean excitatory direction selectivity and inhibitory direction selectivity in each branch. (middle): Difference between mean ipsi-driven excitatory direction selectivity and mean contra-driven excitatory direction selectivity over all synapses on the neuron. (bottom): Direction selectivity index (DSI) calculated for contralateral inputs (purple), ipsilateral inputs (light-green), and binocular inputs (black). See *Model* A_4 in the Methods for the details of evaluation methods. Red vertical lines represent the timing for introduction of inhibitory inputs. Throughout Fig. 7, error bars are standard deviations over 10 simulation trials. **C**) Firing responses of the neuron for monocular inputs, right after the initiation of inhibitory inputs (left; t=30min), and after the learning (right; t=60min). **D**) Examples of direction selectivity of a branch before (gray lines; t=0min) and after (purple/light-green lines; t=60min) the learning. Black lines represent the selectivity of the inhibitory input to the branch. **E**) Behavior in monocular deprivation model. In shadowed areas, to mimic monocular deprivation, contra-driven inputs were replaced with rate-fixed Poisson inputs. Ordinates are the same with Fig. **B**. **F**) Synaptic weights development at different mean inhibitory selectivity. Ordinates are the same with Fig. **B**, and values were calculated at t=60min. Purple and green vertical dotted lines are mean selectivity of contra- and ipsilateral excitatory inputs respectively.